Materials Advances

ROYAL SOCIETY OF CHEMISTRY

PAPER

View Article Online
View Journal | View Issue

Cite this: *Mater. Adv.*, 2025, **6**, 6550

Investigation of the half-metallicity signature and pressure-induced physical properties of cubic $ACrO_3$ (A = Si, Ge, Sn) multiferroic by DFT calculation†

Md. Rony Hossain,[a] Mst. Shamima Khanom,[a] Prianka Mondal *[b] and Farid Ahmed[a]

We report a comprehensive first-principles investigation of the structural, electronic, elastic, magnetic, and optoelectronic properties and half-metallicity of $ACrO_3$ (A = Si, Ge, Sn) with space group *Pm3m* (no. 221), studied for the first time using density functional theory (DFT) in the pressure range of 0–30 GPa. The tolerance factor reveals that the compounds are cubic phase. $SnCrO_3$ is structurally stable. The optimized stable magnetic state of the compounds is ferromagnetic, and by applying Born stability criteria for elastic constants, it is found that $ACrO_3$ (A = Si, Ge, Sn) compounds are mechanically stable over the whole pressure range. The materials' half-metallic nature is confirmed by band gaps and density of states (DOS) studies, which show that the majority spin-channel states are conducting, while the minority spin-down levels are semiconducting. Moreover, we calculated the bulk (B) and shear modulus (G), Poisson's ratio (v), Cauchy pressures, anisotropy (A), plasticity (B/C_{44}) and Young's modulus (E). The plasticity and bond distortion decrease as pressure increases. $SnCrO_3$ and $SiCrO_3$ are brittle at pressures from 0 to 10 GPa, and become ductile in the pressure range of 10 to 30 GPa. In contrast, $GeCrO_3$ is ductile over the whole pressure range. The spin-polarized band structure reveals that $ACrO_3$ (A = Si, Ge, Sn) maintains a direct band gap (R–R) over the whole pressure range. Several optical properties, including dielectric function, reflectivity, refractive index, conductivity, and absorption coefficient, are also calculated. It is revealed from the real part of the dielectric function that the compounds are optically metallic at lower energy and semiconducting at higher energy, and the plasma frequency rises with pressure. The optical properties and half-metallic response show that $ACrO_3$ (A = Si, Ge, Sn) has intriguing properties for spintronic and optoelectronic devices.

Received 21st February 2025,
Accepted 30th June 2025

DOI: 10.1039/d5ma00169b

rsc.li/materials-advances

1. Introduction

Modern electronic devices operate on the principle of electron control, which creates a binary system by considering whether or not electrons are flowing through a circuit. However, the computer industry believes that we have reached the computational limitations of such devices.[1,2] As a result, researchers around the world have been focusing on developing alternatives to conventional electronic devices, with spintronics emerging as a promising choice. Spintronic devices can improve device power by up to ten thousand times thanks to their octane coding based on the electron's spin.[3,4] Emerging technologies require the development of new materials that meet particular requirements. Specifically, magnetic materials with stable structures, good electrical properties, and the potential for thin-film application are needed for spintronic devices.[5,6] The vast majority of materials used in electronic devices are semiconductors. As magnetic behavior can be generated by doping with magnetic species, such materials can be applied in spintronics.[7–9] These materials combine high sensitivity with a remarkable ability to respond to environmental stimuli. Among these, multiferroic materials are an attractive option because they exhibit the coexistence of at least two of the three properties—ferroelectricity, ferromagnetism, and ferroelasticity—due to the interaction of spin, charge, lattice, and orbital degrees of freedom. The magnetoelectric effect, or coupling between electric and magnetic order parameters in multiferroic and magnetoelectric materials, offers an alternate method of electrically controlling the magnetic properties of dielectric materials. Numerous applications of the

[a] *Department of Physics, Jahangirnagar University, Savar, Dhaka, 1342, Bangladesh*
[b] *Dhaka University of Engineering & Technology, Gazipur, 1707, Bangladesh. E-mail: priankamondal6@yahoo.com*

† Electronic supplementary information (ESI) available. See DOI: https://doi.org/10.1039/d5ma00169b

magnetoelectric effect have been proposed, such as modulators,[10] field sensors, energy and frequency converters,[11] transformers and gyrators, transducers and memory devices,[12] and signal amplifiers.[13] They have fascinating application possibilities in contemporary electronics and information technology, particularly in electromagnetic sensors and magnetic storage media. The development, performance enhancement, and use of multiferroic materials have emerged as critical areas of study for strongly correlated electronic systems and spintronics.[14]

A half-metallic compound exhibits the behaviors of both an insulator or a semiconductor in one spin channel and a metal in other spin channel.[15,16] de Groot *et al.*[17] first introduced the idea of half-metallic compounds. This hybrid behavior culminates in complete (100%) spin polarization at the Fermi level. Subsequently, these substances generate spin-polarized currents, enhancing the efficiency of magnetoelectronic devices. Numerous materials have been proven to be half-metals, including transition metal pnictides and metal chalcogenides,[18] oxides,[19,20] Heusler alloys,[21] graphene nanoribbons,[22] spinel ferrites,[23] and zinc blende magnetic semiconductors.[24] These magnetic materials have found significant applications in the field of spintronics.[25] However, more research is needed on half-metallicity signatures in multiferroic materials. ABO_3-type materials have been extensively studied for various technological applications—such as ferroelectric devices, gas sensors, and actuators—due to their ability to exhibit diverse physical and chemical properties, which depend on the specific metal atoms present at the A and B positions.[26] $BiFeO_3$, the most well-known multiferroic (MF) compound, has drawn much attention in recent decades due to its multiferroic characteristics; it exhibits a remarkable combination of electronic, optical, magnetic, and ferroelectric properties and can be readily synthesized *via* epitaxial growth on $SrTiO_3$ substrates. Other notable MF compounds include $YMnO_3$, $BiMnO_3$, $PbNiO_3$, $FeTiO_3$, $PbVO_3$, $YMnO_3$, $TbMn_2O_5$, Ca_3CoMnO_6, $LuFe_2O_4$, and $BaNiF_4$.[27–33] Jena *et al.*[34] investigated $BiFeO_3$ using DFT-based first-principles calculations using the pseudopotential method implemented in the Quantum Espresso (QE) package. They reported that the tetragonal phase goes through a half-metallic phase before evolving from a ferromagnetic semiconductor to a ferromagnetic metal as the c/a ratio drops from 1.264 to 1.016. The half-metallic phase in X = B/C/N/F-doped $KNbO_3$ was explored by Anar and Nazir.[35] They also looked into the band gap and estimated the Curie temperature in magnetically doped structures using the Heisenberg 2D Hamiltonian model, and they discovered that the temperature was high enough to be useful for practical purposes. Fang *et al.*[36,37] investigated the magnetic properties of $BaMnO_3(Ba_{1/3}Sr_{1/3}Ca_{1/3})TiO_3$ and reported the existence of half-metallic properties using DFT. Using the LSDA+U scheme, Zhu *et al.*[38] investigated the half-metallic nature of the cubic $BaCrO_3$ structure and showed that the $BaCrO_3$ superlattice is a more stable interface than $BaCrO_3$. Ghosh *et al.*[39,40] conducted an experimental study on bismuth ferrite ($BiFeO_3$) and confirmed its ferromagnetic nature using X-ray photoelectron spectroscopy (XPS). Their findings were also validated by density functional theory (DFT+U), confirming that this material is feasible for spintronics applications. Recent studies on multiferroic (MF) materials have largely concentrated on modification strategies such as doping, co-doping, heterojunction engineering, the development of double-perovskite structures, and the tuning of intrinsic properties. In addition to these approaches, both experimental and theoretical efforts have been directed toward understanding key physical characteristics, including optical, vibrational, and elastic behavior. Among the theoretical methods, computational chemistry, particularly density functional theory (DFT), has proven to be a highly effective tool, offering a favorable balance between computational costs and predictive accuracy.[27,28] DFT, which is grounded in the Kohn–Sham formalism and incorporates the exchange–correlation functional, enables accurate modeling of the electronic structure and related properties. In this work, the B3LYP hybrid functional has been adopted owing to its demonstrated reliability and flexibility in the study of complex oxide systems.

To the best of our knowledge, there have been no prior theoretical or experimental investigations of the physical properties of $ACrO_3$ (A = Si, Ge, Sn) multiferroic compounds. Understanding these materials is important, as multiferroics with tunable properties are of great interest for advanced electronic and spintronic applications. Our work aims to fill this gap by systematically investigating and comparing the structural, mechanical, electronic, and optical properties of $ACrO_3$ (A = Si, Ge, Sn) compounds under ambient and high-pressure conditions (up to 30 GPa). Such pressure-dependent studies can reveal important insights into the band gap behavior and Curie temperature evolution, which are crucial for designing materials that function reliably at higher temperatures. Therefore, this study provides both a novel theoretical foundation and potential practical implications for the design of future multifunctional devices, particularly in the fields of spintronics and high-pressure electronics.

2. Computational details

The DFT-based CASTEP computer software with the generalized gradient approximation (GGA) was used for first-principles calculations. The Perdew–Burke–Ernzerhof (PBE) exchange–correlation functional with projected augmented-wave (PAW) pseudopotentials was selected for the calculations,[41–43] and O-$2s^2\ 2p^4$, Cr-$3s^2\ 3p^6\ 3d^5\ 4s^1$, Si-$3s^2\ 3p^2$, Ge-$3d^{10}\ 4s^2\ 4p^2$, and Sn-$4d^{10}\ 5s^2\ 5p^2$ were used as valence electrons. For the lattice optimization, the convergence parameters were set as follows: (i) maximum ionic displacement of 0.002 Å, (ii) maximum stress component of 0.10 GPa, and (iii) maximum ionic force of 0.05 eV $Å^{-1}$. The electromagnetic wave function extension in a plane-wave basis set uses an energy cut-off of 400 eV, and the Brillouin zone is sampled using $8 \times 8 \times 8$ k-points for all calculations. The Broyden method was applied to optimize the geometric structure using the Fletcher–Goldfarb–Shanno (BFGS) minimization technique.[44] The Vanderbilt-type ultrasoft

pseudopotential (UPP) formalism was used to analyze the interactions between valence electrons and ions. UPPs achieve a substantially softer pseudo-wave function, requiring a significant reduction in plane waves for calculations with the same level of precision.[45] Additionally, spin polarization was only applied to the magnetic state in the lowest energy computation, and spin polarization was not applied to the non-magnetic state in all other computations. The elastic constants were determined using first-principles computations by carrying out a sequence of specified homogeneous distortions with finite parameters and calculating the resulting stress by optimizing the interior atomic freedom. With an upper limit of 0.5%, each strain element had three positive and three negative amplitudes. After that, the calculated stress as a function of strain was fitted linearly to obtain the elastic modulus. To facilitate the calculation of the optical properties for a dense mesh of evenly distributed *k*-points, BZ integration was performed using a 12 × 12 × 12 MP *k*-mesh.

3. Results and discussion

3.1. Ground state structural features

$ACrO_3$ (A = Si, Ge, Sn) adopts a cubic structure with the $Pm\bar{3}m$ space group, as shown in Fig. 1. These structures are optimized in ferromagnetic (FM) and non-magnetic (NM) states to verify the most stable state. All the investigated compounds are more stable in the ferromagnetic state, as shown in Table 1.

To investigate how pressure affects the crystal structure of $ACrO_3$ (A = Si, Ge, Sn), we examined the variation in unit cell volume and lattice constant under pressures ranging from 0 to 30 GPa. The results in Fig. 3(a) and (b) indicate that the lattice constant and volume decrease as pressure increases, although they do not decrease at the same rate. As pressure increases, the ratios of a/a_0 and the normalized volume V/V_0, where V_0 and a_0 stand for the volume at zero pressure, and the equilibrium lattice parameter decrease, as shown in Fig. 3(c). This normalization allows for a more precise comparison of how much the lattice parameter and volume change with pressure. Fig. 3 provides a comprehensive view of how $ACrO_3$ (A = Si, Ge, Sn) responds to applied pressure, confirming that the material retains its cubic phase while exhibiting significant changes in its structural parameters.

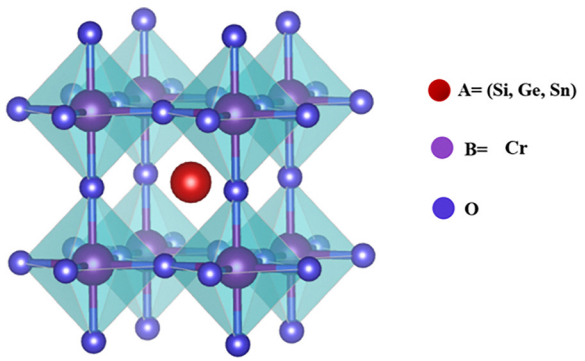

Fig. 1 The cubic crystallographic unit cell of $ACrO_3$ (A = Si, Ge, Sn).

We also calculated the cohesive energy (E_{coh}) of the ABO_3 compounds to explore more about their structure stability using the equation:[46]

$$E_{coh} = \left[E_A^{iso} + E_{B(Cr)}^{iso} + 3E_O^{iso}\right] - E_{ABO_3}^{Total} \quad (1)$$

where $E_{ABO_3}^{Total}$ is the total equilibrium energy of ABO_3 and E_A^{iso}, $E_{B(Cr)}^{iso}$ and E_O^{iso} are the energies of the isolated atoms, respectively.

A material with high cohesive energy is more stable due to stronger bonds (*e.g.*, ionic, covalent) that require more energy to break. High cohesive energy correlates with greater hardness, strength, and resistance to deformation, as well as tightly bound electrons that influence conductivity and electronic properties. These results suggest that pressure has a non-linear effect on the cohesive energy of $ACrO_3$ (A = Si, Ge, Sn) compounds as shown in Fig. 2. The initial reduction in cohesive energy under pressure could be due to increased repulsion or distortion in the lattice. The slight recovery at higher pressures may indicate a more compact or stabilized structure. All of our compounds possess high cohesive energy, so we can infer that they are more resistant to mechanical stress and chemical corrosion, making them suitable for harsh environments (Table 2).

3.2. Bonding analysis

The atomic charges, chemical bond lengths, and bond populations determined using the Mulliken technique are displayed in Table 3. Regarding the O atoms, the charge transfer from the A (= Si, Ge, Sn) and Cr atoms is around 0.90, 1.22, 1.06 and 0.94 electrons, respectively. The minimum and maximum values for the bond populations suggest that the chemical bond has strong iconicity and covalency, respectively.[47,48] Consequently, we conclude that $ACrO_3$ (A = Si, Ge, Sn) exhibits covalent and ionic bonding behavior. Table 3 displays the predicted O–A (A = Si, Ge, Sn) and Cr–O bond lengths based on Mulliken population analysis. A multiferroic compound tolerance factor can be determined by measuring the bond lengths between the constituent atoms, which allows for the identification of the crystal symmetry given by ref. 49:

$$t = \frac{0.707(A - O)}{(Cr - O)} \quad (2)$$

where (A–O) and (Cr–O) are the bond lengths. The computed tolerance factors are 0.97, 1.009, and 0.999 for $SiCrO_3$, $GeCrO_3$, and $SnCrO_3$, respectively. The compounds all fall within the range of 0.93–1.02,[50] which validates that they are cubic.

3.3. Electronics properties

A thorough understanding of a material's electronic structure is essential for determining its potential applications across various fields of scientific research. The energy band gap, in particular, plays a key role in defining the suitability of a material for use in smart devices, spintronics, and memory technologies. Furthermore, theoretical quantum-level analyses provide detailed insights into the electronic nature of materials. Based on their electronic properties, materials can be

Table 1 Calculated lattice constant a (A), equilibrium volume V_0, normalized lattice parameter, and volume cubic $ACrO_3$ (A = Si, Ge, Sn) multiferroic compounds at different pressure

Compound	Parameter	0 GPa	10 GPa	20 GPa	30 GPa
$SiCrO_3$	Energy E_{FM} (eV)	−3885.06	−3884.90	−3884.77	−3884.68
	Energy E_{NM} (eV)	−3884.74	−3884.74	−3884.64	−3884.47
	Spin-polarized lattice constant a (A)	3.79	3.70	3.65	3.60
	Non-spin-polarized lattice constant a (A)	3.75	3.69	3.65	3.61
	Volume (FM) V_0	54.57	50.52	48.79	46.93
	Volume (NM) V_0	53.07	50.49	48.73	47.11
	Normalized lattice parameter a/a_0	1	0.97	0.96	0.94
	Normalized volume V/V_0	1	0.92	0.89	0.85
$GeCrO_3$	Energy E_{FM} (eV)	−6253.95	−6253.88	−6253.76	−6253.70
	Energy E_{NM} (eV)	−6253.75	−6253.71	−6253.62	−6253.57
	Spin-polarized lattice constant a (A)	3.81	3.74	3.69	3.66
	Non-spin-polarized lattice constant a (A)	3.78	3.72	3.67	3.63
	Volume (FM) V_0	55.63	52.72	50.58	49.09
	Volume (NM) V_0	54.40	51.58	49.61	47.94
	Normalized lattice parameter a/a_0	1	0.98	0.968	0.960
	Normalized volume V/V_0	1	0.94	0.90	0.88
$SnCrO_3$	Energy E_{FM} (eV)	−5765.26	−5765.08	−5764.89	−5764.56
	Energy E_{NM} (eV)	−5764.98	−5764.89	−5764.74	−6764.44
	Spin-polarized lattice constant a (A)	3.87	3.81	3.72	3.68
	Non-spin-polarized lattice constant a (A)	3.84	3.77	3.72	3.68
	Volume (FM) V_0	58.29	55.60	51.78	49.85
	Volume (NM) V_0	56.91	53.95	51.77	49.85
	Normalized lattice parameter a/a_0	1	0.98	0.96	0.950
	Normalized volume V/V_0	1	0.953	0.88	0.855

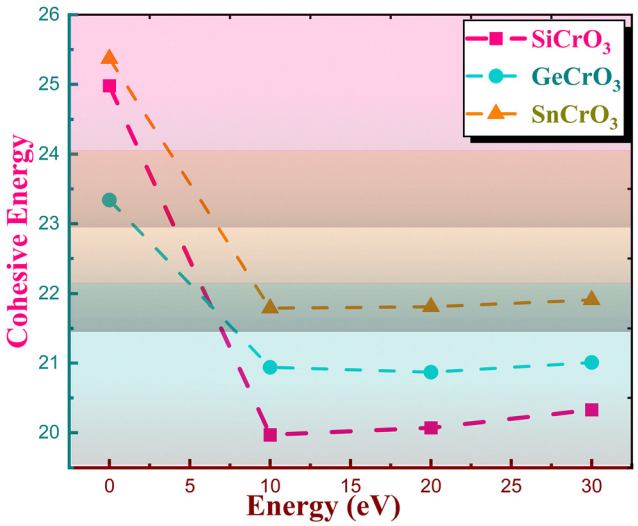

broadly classified as metals, insulators, semiconductors, spin-gapless semiconductors, half-metals, and more.[51] The electronic properties of a material are determined by the contributions of various electronic states in the valence and conduction bands. Understanding the electrical structure is crucial for providing helpful information regarding their experimental modeling and potential use in fabricating numerous energy devices. It has been reported that GGA typically underestimates the electronic band gap, especially in the case of semiconductors and insulators. This discrepancy is primarily explained by the GGA functional's simplicity and the lack of the necessary flexibility to precisely capture exchange–correlation energy, which results in a comparatively lower electronic band gap energy value. Therefore, we studied the band structure, DOS and PDOS using the GGA+U functional.[52] The electrical band structures of $ACrO_3$ (A = Si, Ge, Sn) at varying pressures are shown in Fig. 4. Fig. 4 indicates that the top of the valence band (VB) and the bottom of the conduction band (CB) do not overlap; both occur at the R symmetry point. This suggests that $ACrO_3$ (A = Si, Ge, Sn) exhibits half-metallic behavior.

It has been discovered that under ambient conditions, the top of the VB and the bottom of the CB are located at the R symmetry point. Remarkably, it was found that for $SnCrO_3$, elevating the pressure caused the top of the VB at the R and Γ symmetry locations to move closer to the Fermi level and at 20 and 30 GPa, the top of the valence band at the R and Γ symmetry points crosses the Fermi level. Conversely, no relative shift was seen when looking at the band structures of $SiCrO_3$ and $GeCrO_3$, suggesting that the electrical characteristics of these materials are stable under external pressure. Due to this

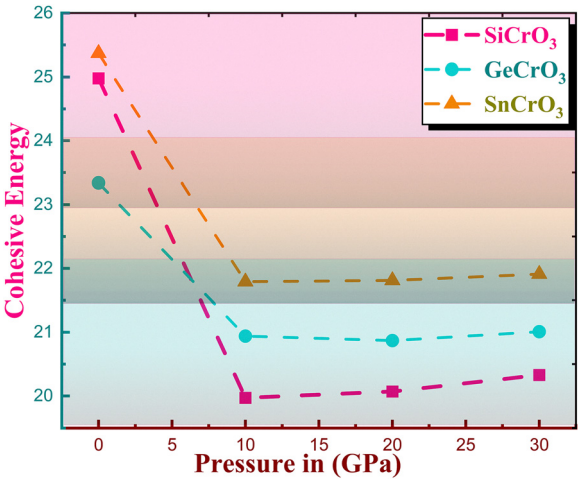

Fig. 2 Cohesive energy of cubic $ACrO_3$ (A = Si, Ge, Sn) compounds at different pressure.

band structure stability, $SiCrO_3$ and $GeCrO_3$ may retain consistent electrical conductivity and other electronic properties. Closely examining Fig. 4 reveals that the energy band edges at the *R* and *Γ* points have flat bands, while the remaining points exhibit slightly bouncy curvature. This indicates that $ACrO_3$ (A = Si, Ge, Sn) has higher effective masses at the *L* and *Γ* points than at other locations.[53]

The spin-polarized total and partial DOS, displayed in Fig. 5 and 6, explain contributions of various electronic states to the band structure. When considering the spin-up channel, the $ACrO_3$ (A = Si, Ge, Sn) compounds possess occupied states at the Fermi level and show metallic characteristics. Conversely, $ACrO_3$ (A = Si, Ge, Sn) exhibits semiconducting behavior for the spin-down channel and unoccupied states at the Fermi level. Fig. 5 shows that as the pressure is increased to 30 GPa, the conduction bands move downward, the valence bands shift upward, and the band gap eventually contracts for $SiCrO_3$ and $SnCrO_3$. Fig. 5 indicates that at 30 GPa, there is no band gap at the Fermi level, and the material exhibits metallic behavior. Thus, $SiCrO_3$ and $SnCrO_3$ undergo a phase shift at 30 GPa. The semiconducting gap in $GeCrO_3$ is almost constant throughout the pressure range, suggesting that the electronic bandgap is highly stable and is not affected by variations in pressure.

Table 2 The cohesive energy of cubic $ACrO_3$ (A = Si, Ge, Sn) multiferroic compounds at different pressure

	Structure	0 GPa	10 GPa	20 GPa	30 GPa
Cohesive energy	$SiCrO_3$	24.98	19.97	20.07	20.33
	$GeCrO_3$	23.34	20.94	20.87	21.01
	$SnCrO_3$	25.37	21.79	21.81	21.91

Fig. 6 clearly shows that in the spin-up channel, the O-2p state contributes to the bottom of the VB at −2.4 eV, while the Cr-3d state at the Fermi level contributes significantly. The plot indicates that the hybridization of O-2p and Cr-3d states is responsible for the top of the VB and that this hybridization contributes more to the spin-up channel than the spin-down channel, making the $ACrO_3$ (A = Si, Ge, Sn) compounds metallic in the spin-up channel. Interestingly, the O-2p state at the bottom of the valence band drifts leftwards with increasing pressure. In the CB, the highest contribution comes from the Sn-s state at 2.2 eV and the O-2p state at 4.5 eV. In the case of a down channel, polarization occurs at the Fermi level, and the 3d state of the Cr atom jumps into the CB and is localized at 2.2 eV.

3.4. Spin magnetic moment and spin polarization

The temperature at which spontaneous magnetization in magnetic material ceases is called the Curie temperature, sometimes referred to as the Curie point or the magnetic transition point. The Curie temperature is calculated using the Heisenberg mean field approximation:[54]

$$T_C = \frac{\Delta E}{3k_B} \quad (3)$$

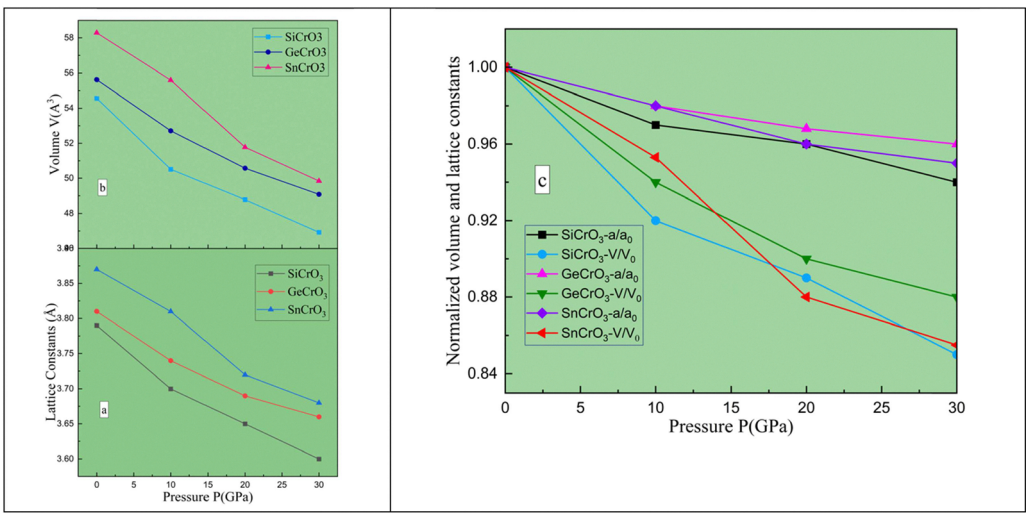

Fig. 3 Variation of (a) lattice parameter, (b) cell volume and (c) normalized lattice parameter and volume of $ACrO_3$ (A = Si, Ge, Sn) as a function of pressure.

Table 3 Mulliken charges, bond lengths, and bond populations analysis of $ACrO_3$ (A = Si, Ge, Sn) obtained using the GGA method

	Species	s	P	d	Total	Charge (electron)	Bond	Population	Bond length (Å)	Tolerance factor (t)
$SiCrO_3$	Si	2.04	1.06	0	3.10	0.90	O–Si	0.03	2.60	0.97
	Cr	2.28	6.39	4.44	13.10	0.89	O–Cr	0.85	1.88	
	O	1.85	4.75	0	6.60	−0.60				
$GeCrO_3$	Ge	1.71	1.07	10	12.78	1.22	O–Ge	−0.16	2.69	1.009
	Cr	2.44	6.58	4.31	13.33	0.67	O–Cr	1.05	1.90	
	O	1.85	4.78	0	6.63	−0.63				
$SnCrO_3$	Sn	1.98	0.95	10.0	12.94	1.06	O–Sn	0.06	2.74	0.999
	Cr	2.31	6.45	4.30	13.06	0.94	O–Cr	0.82	1.93	
	O	1.85	4.82	0	6.67	−0.67				

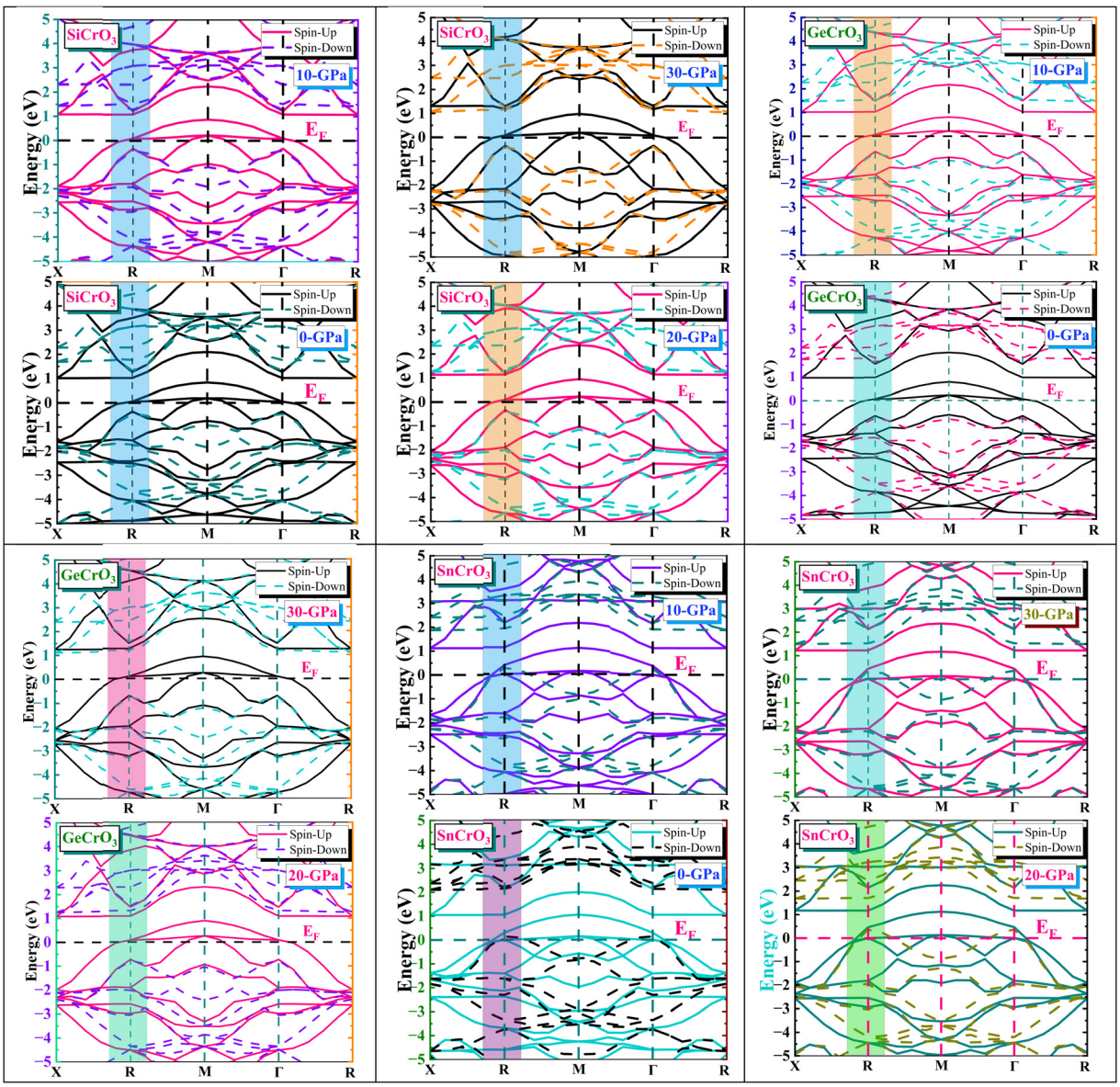

Fig. 4 Predicted spin-polarized band structures of $ACrO_3$ (A = Si, Ge, Sn) under hydrostatic pressure of 0–30 GPa using the GGA+U functional.

where ΔE is the energy difference between non-magnetic E_{NM} and ferromagnetic state E_{FM} and represents the energy barrier that must be overcome to transition from the non-magnetic to the ferromagnetic state. Fig. 7 illustrates that the Curie temperature did not fall linearly with pressure but rapidly decreased, especially for $SiCrO_3$, which fell faster than

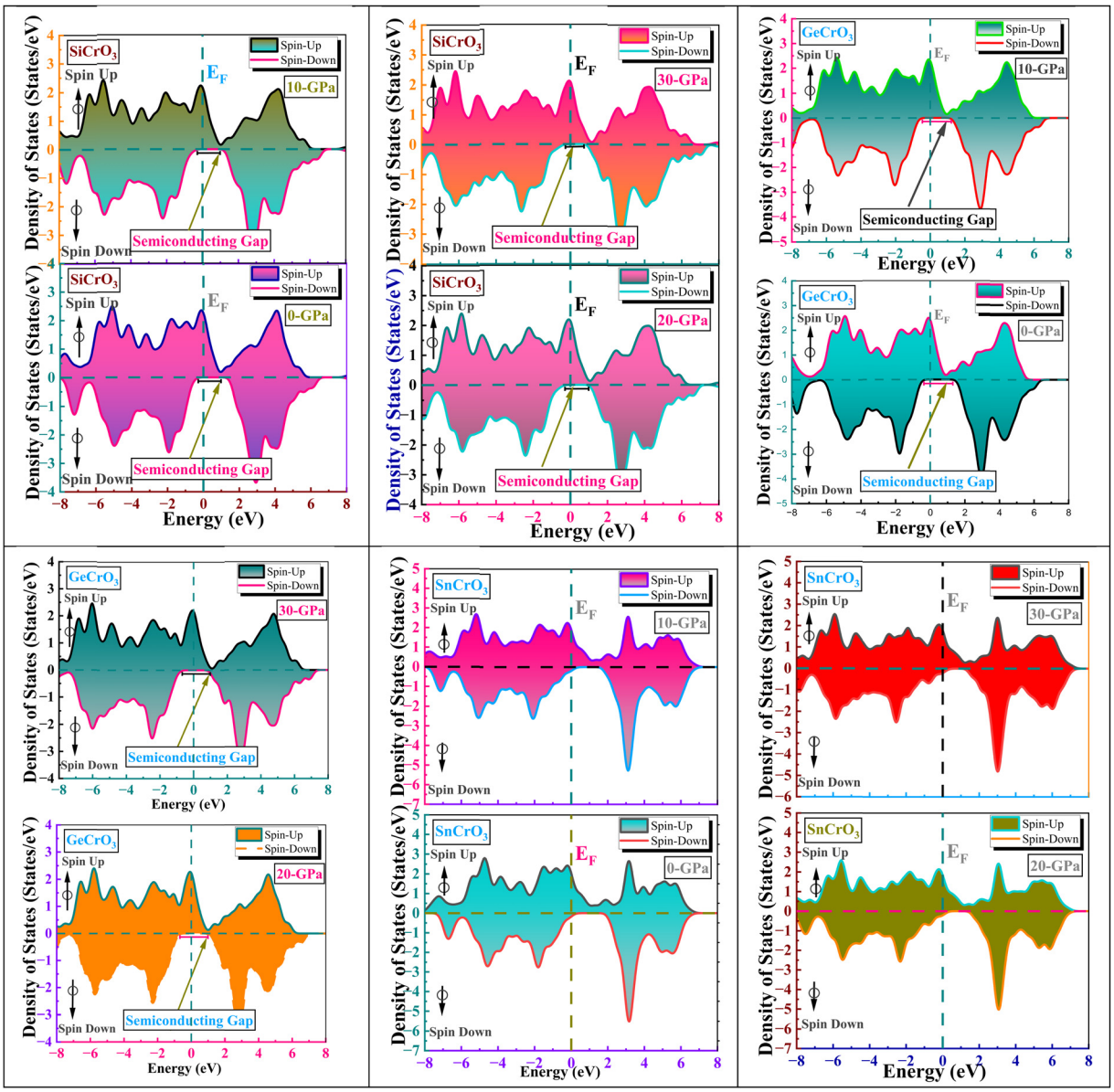

Fig. 5 Density of states (DOS) for GGA in the cubic structure of $ACrO_3$ (A = Si, Ge, Sn).

the other investigated compounds. Leger *et al.*[55] investigated the effect of pressure on the T_C of alloys with transition atoms and found similar trends, so our results are consistent with the literature. We found that the Curie temperatures at normal pressure are 1236.71 K, 772.94 K, and 1082.12 K for $ACrO_3$ (A = Si, Ge, Sn) compounds, respectively, which are relatively higher than room temperature and only seen in full-Heusler alloys.[56] $ACrO_3$ (A = Si, Ge, Sn) has a high Curie temperature, making it a promising material for spintronics applications[57] (Fig. 8).

At T = 0 K, the spin-polarized computation directly obtains the magnetic moment. Utilizing the actual magnetic moments per formula unit, the magnetic moment is calculated as follows:

$$\mu = 3O_{oxygen} + Cr + A(Sn, Ge, Si) \quad (4)$$

The calculated magnetic moment is listed in Table 4, and it is observed that at pressure up to 10 GPa, the total magnetic moment is almost the same for all the compounds. However, above 10 GPa, the total magnetic moment changed for $SnCrO_3$. Additionally, we looked into how pressure affects the magnetic moment per atom of each of the three compounds between 0 and 30 GPa. Moulay *et al.*'s[58] investigation of the pressure dependence of magnetic moments for multiferroic compounds revealed that the individual elements' magnetic moments do not significantly change in response to pressure.

The constant compression of its lattice directly impacts the physical characteristics of a material. These characteristics influence the compound's magnetic, structural, electrical, and optical qualities. The robust shift lattice parameter (RTLC) is the critical lattice parameter at which the total magnetic

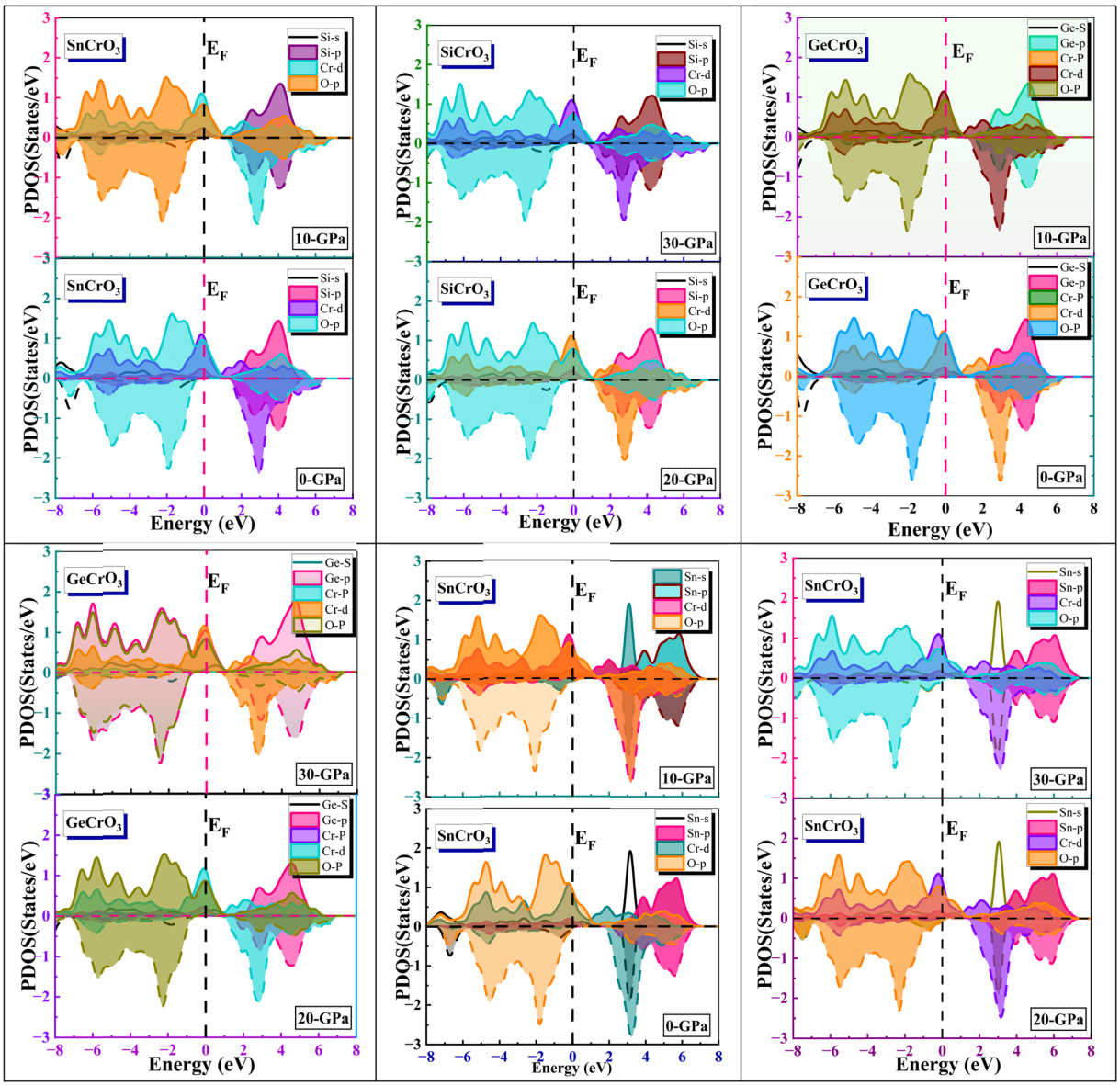

Fig. 6 Spin-polarized partial density of states (PDOS) of cubic $ACrO_3$ (A = Si, Ge, Sn) at various pressures.

moment of a half-metal substance abruptly shifts to a non-integer value, and the electronic nature of the compound changes from half-metal to metal at that lattice parameter, making it a fundamental lattice constant to study.[59] Fig. 9 shows that the magnetic moment for $SnCrO_3$ changed from an integer ($\cong 1.99\mu_B$) to a non-integer value as the lattice constant decreased with an increase in external pressure. At 3.78 Å, there is a sudden transition, and the compound loses its integer magnetic moment ($2\mu_B$ to $0.50\mu_B$). This sudden shift verifies that the robust lattice constant for $SnCrO_3$ is 3.78 Å.

The spin polarization of $ACrO_3$ (A = Si, Ge, Sn) is reflected by the bandgap present at the Fermi level, which is essentially the difference in spin density between the spin-up and -down channels near the Fermi level (E_F). Spin polarization can be obtained from the following relation:

$$\text{Spin polarization} = \frac{N\uparrow(E_F) - N\downarrow(E_F)}{N\uparrow(E_F) + N\downarrow(E_F)} \quad (5)$$

where $N\uparrow(E_F)$ and $N\downarrow(E_F)$ are the DOS for the spin-up and spin-down channels near the Fermi level, respectively. For these two channels, when any of the states of the Fermi level is zero, 100% spin polarization will occur. From the band diagram, it is observed that the DOS along the down channel near the Fermi level is zero, which makes $ACrO_3$ (A = Si, Ge, Sn) a half-metallic material (Table 4).

3.5. Mechanical properties

Elastic constants are necessary to obtain a more thorough theoretical comprehension of the characteristics of materials

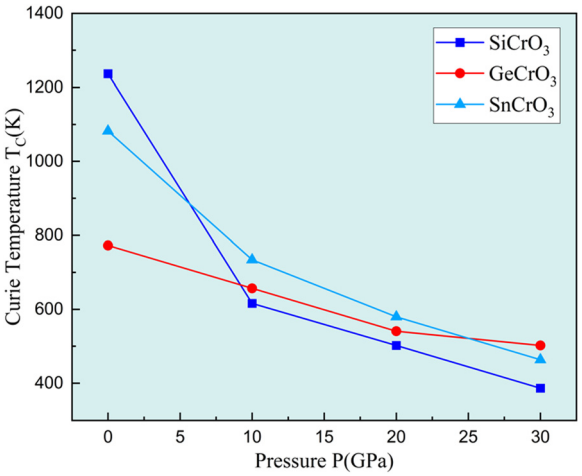

Fig. 7 The relation between Curie temperature and pressure.

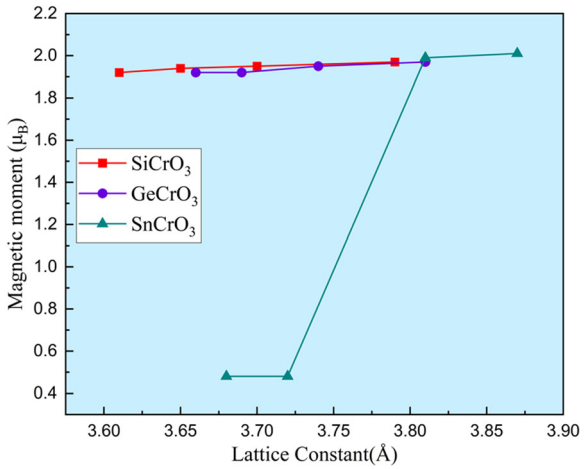

Fig. 9 Spin moment *versus* lattice constants for $ACrO_3$ (A = Si, Ge, Sn) compounds

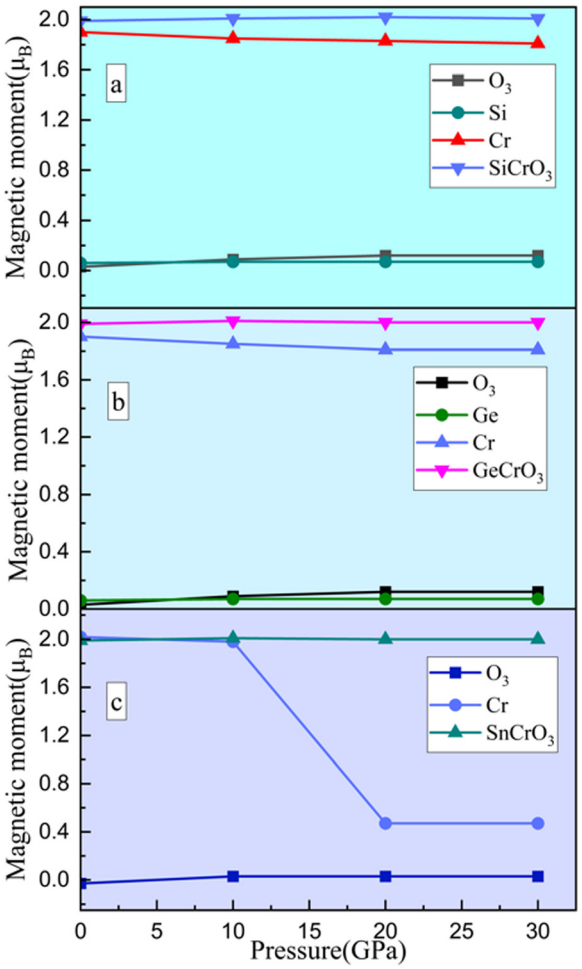

Fig. 8 Effect of pressure on the magnetic moments at O_3, Cr, Si, Ge, and Sn atomic sites for $ACrO_3$ (A = Si, Ge, Sn) multiferroic materials in GGA calculations.

Table 4 Spin magnetic moment and Curie temperature of $ACrO_3$ (A = Si, Ge, Sn) at various pressures

	Magnetic moment	0 GPa	10 GPa	20 GPa	30 GPa
$SiCrO_3$	Moment μ_O	0.03	0.09	0.12	0.12
	Moment μ_{Si}	0.06	0.07	0.07	0.07
	Moment μ_{Cr}	1.90	1.85	1.83	1.81
	Total μ	1.99	2.01	2.02	2.01
	Curie temperature T_C (K)	1236.71	616.35	502.41	386.47
$GeCrO_3$	Moment-μ_O	0.03	0.09	0.12	0.12
	Moment-μ_{Ge}	0.06	0.07	0.07	0.07
	Moment-μ_{Cr}	1.90	1.85	1.81	1.81
	Total μ	1.99	2.01	2.0	2.0
	Curie temperature T_C (K)	772.94	657	541.06	502.41
$SnCrO_3$	Moment μ_O	−0.03	0.03	0.03	0.03
	Moment μ_{Sn}	0	0	0	0
	Moment μ_{Cr}	2.02	1.98	0.47	0.47
	Total μ	1.99	2.01	0.50	0.50
	Curie temperature T_C (K)	1082.12	734.29	579.70	463.76

that are determined by the electron–phonon interaction processes and the DOS of phonons. As the stress–strain curve in many minerals exhibits low nonlinearity, practical applications can assume a linear relationship between stress and strain.[60] Elastic constants can be used to calculate essential physical parameters like melting point, hardness, sound velocities, Debye temperature, and shear modulus. The elastic constants are the total energy second derivative for different lattice deformations. More thorough computations of the total energy are necessary[61] for the elastic constants. The elastic constants can be calculated from the formula:

$$C_{ij} = \frac{1}{V_0}\left(\frac{d^2E}{de_ie_j}\right) \quad (6)$$

where E is the internal energy, V_0 indicates the equilibrium volume, and e_i and e_j are the stress and strain components.

As $ACrO_3$ (A = Si, Ge, Sn) is a cubic structure with a high degree of symmetry, the elastic constant reduces to three independent elastic constants: C_{11}, C_{12}, and C_{44}.[62] The following is an expression of the conventional mechanical stability

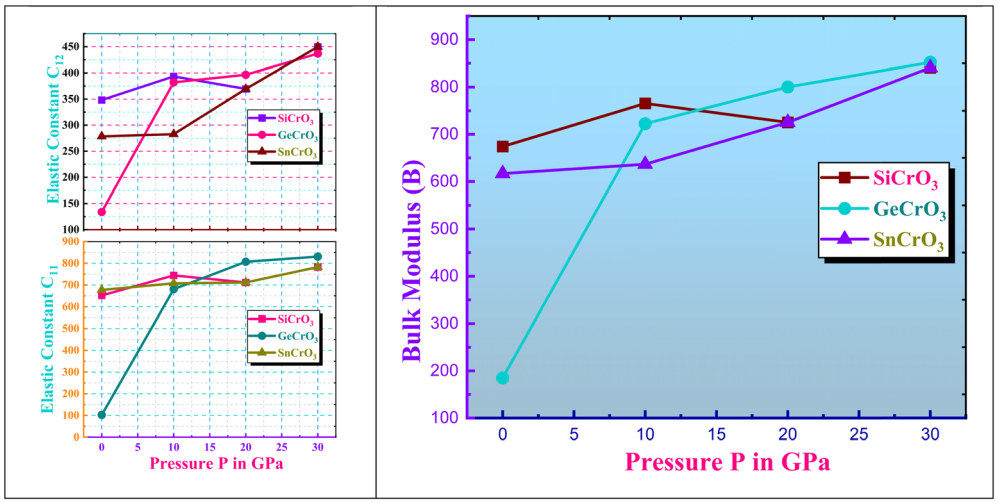

Fig. 10 Elastic constant (left) and bulk modulus (right) of $ACrO_3$ (A = Si, Ge, Sn) at different hydrostatic pressures.

conditions in cubic crystals at equilibrium in terms of elastic constants:[63,64]

$$C_{44} > 0,\ C_{11} > |C_{12}|,\ C_{11} + 2C_{12} > 0 \quad (7)$$

The equations for mechanical stability under pressure are given by ref. 65:

$$C'_{11} - C'_{12} = (C_{11} - C_{12}) - 2P > 0,\ C'_{11} + 2C'_{12} = (C_{11} + 2C_{12}) \to 0,\ C'_{44} = C_{44} - P > 0 \quad (8)$$

From the data reported in Table 5, the dynamic stability of the compounds $ACrO_3$ (A = Si, Ge, Sn) was assessed using pressure-modified elastic criteria. $SiCrO_3$ and $SnCrO_3$ are dynamically stable at 0, 10, and 30 GPa, but both exhibit instability at 20 GPa, primarily due to a negative $C_{44} - P$, indicating shear softening under pressure. In contrast, $GeCrO_3$ is unstable at ambient pressure but becomes dynamically stable at pressures above 10 GPa, suggesting pressure-induced stabilization. The bulk modulus (B), shearing modulus (G), Young's modulus (E), anisotropy (A), Poisson's ratio (ν), Pugh's ratio (B/G), plasticity measurement (B/C_{44}), and Kleinman parameter (ς) were calculated using the following expressions, respectively:[66–70]

$$B = \frac{1}{3}(C_{11} + 2C_{12}) \quad (9)$$

$$G = \frac{G_V + G_R}{2} \quad (10)$$

$$G_V = \frac{C_{11} - C_{12} + C_{44}}{5} \quad (11)$$

$$G_R = \frac{5C_{44}(C_{11} - C_{12})}{4C_{44} + 3(C_{11} - C_{12})} \quad (12)$$

$$E = \frac{9BG}{(3B + G)} \quad (13)$$

$$A = \frac{2C_{44}}{C_{11} - C_{12}} \quad (14)$$

$$\nu = \frac{(3B - 2G)}{2(3B + G)} \quad (15)$$

$$\zeta = \frac{C_{11} + 8C_{12}}{7C_{11} + 2C_{12}} \quad (16)$$

As the shear modulus indicates the rigidity of a compound, the mechanical failure in $ACrO_3$ (A = Si, Ge, Sn) should be revealed by the shear component under the criteria $G < B$ in this case. The bulk modulus of a material determines the counteraction against the volume change due to applied pressure, compared to the shear modulus, which defines the counteraction against plastic distortion.[71] The bulk modulus values of $SiCrO_3$, $GeCrO_3$ and $SnCrO_3$ exhibit a clear increasing trend with applied pressure, indicating enhanced resistance to volume compression. For $SiCrO_3$, the bulk modulus increases from 674.13 GPa at 0 GPa to 840.77 GPa at 30 GPa, suggesting improved mechanical rigidity under compression. $GeCrO_3$ shows a substantial increase from 185.12 GPa to 852.15 GPa over the same pressure range, which may indicate a pressure-induced structural stabilization. In the case of $SnCrO_3$, the bulk modulus rises steadily from 616.97 GPa to 840.77 GPa, reflecting consistent stiffening behavior under pressure. The stiffness of a solid can be determined by calculating its Young's modulus (E), which is the ratio of tensile stress to tensile strain, and a low E value indicates greater plasticity. In the current investigation, the Young's modulus (E) for $GrCrO_3$ and $SnCrO_3$ is relatively low at 0 and 10 GPa, and the compounds significantly lose flexibility at higher pressures. Conversely, $SiCrOSiCrO_3$ has a maximum value at pressure of 10 GPa.

Poisson's ratio, also known as the transverse deformation coefficient, is an elastic constant that describes how a material deforms sideways in response to longitudinal force. Poisson's ratio is a characteristic with a minimum value of approximately 0.25[72] in most metals. We can infer the ductile or brittle behaviors of GeCrO, SiCrO, and SnCrO under various pressure situations from Fig. 11. The graph illustrates how each compound responds differently to pressure variations. All of the

Table 5 Bulk modulus B (GPa), shear modulus G (GPa), Young's modulus E (GPa), hardness (GPa), plasticity measurement (B/C_{44}), Pugh's ratio (B/G), ($C_{11}-C_{44}$) Cauchy pressure (GPa), Poisson's ratio (ν), Kleinman parameter (ζ) and Zener anisotropy factor (A) of $ACrO_3$ (A = Si, Ge, Sn)

Compound	Elastic parameters	0 Pa	10 Gpa	20 Gpa	30 Gpa
$SiCrO_3$	C_{11}	651.77	744.04	711.45	782.30
	C_{12}	348.24	393.47	369.52	449.62
	C_{44}	60.88	68.21	2.47	56.31
	Bulk modulus (B)	674.12	765.49	725.24	840.77
	Shear modulus (Voigt) G_V	72.88	83.75	68.88	77.79
	Shear modulus (Reuss) G_R	80.05	90.26	4.07	76.56
	Shear modulus (Hill) G	76.46	87.01	36.47	77.18
	Young's modulus (Hill) E	221.05	251.50	107.63	224.67
	Cauchy pressure ($C_{12}-C_{44}$)	287.36	325.26	367.05	393.31
	Kleinman parameter (ζ)	0.65	0.64	0.64	0.68
	Pugh's ratio (B/G)	8.81	8.79	19.88	10.89
	Poisson ratio (ν)	0.44	0.44	0.47	0.45
	Plasticity measurement (B/C_{44})	11.07	11.22	293.62	14.93
	Anisotropy factor (A)	0.40	0.38	0.01	0.33
	Dynamic stability	Stable	Stable	Unstable	Stable
$GeCrO_3$	C_{11}	102.49	680.65	806.98	830.71
	C_{12}	133.87	382.18	396.60	436.79
	C_{44}	75.06	89.95	85.52	86.39
	Bulk modulus (B)	185.11	722.5	800.09	852.14
	Shear modulus (Voigt) G_V	8.73	77.68	99.18	96.06
	Shear modulus (Reuss) G_R	−57.18	106.94	111.54	111.14
	Shear modulus (Hill) G	−24.20	92.31	105.36	103.73
	Young's modulus (Hill) E	−75.91	265.62	302.79	299.06
	Cauchy pressure ($C_{12}-C_{44}$)	58.81	292.23	311.08	350.4
	Kleinman parameter (ζ)	1.19	0.67	0.61	0.64
	Pugh's ratio (B/G)	−7.64	7.82	7.59	8.21
	Poisson ratio (ν)	0.56	0.43	0.43	0.44
	Plasticity measurement (B/C_{44})	2.46	8.03	9.35	9.86
	Anisotropy factor (A)	−4.78	0.6	0.41	0.43
	Dynamic stability	Stable	Stable	Stable	Stable
$SnCrO_3$	C_{11}	677.05	707.66	711.45	782.30
	C_{12}	278.44	282.71	369.52	449.62
	C_{44}	126.53	92.78	2.47	56.31
	Bulk modulus (B)	616.96	636.54	725.24	840.77
	Shear modulus (Voigt) G_V	105.02	103.54	68.88	77.79
	Shear modulus (Reuss) G_R	148.17	119.76	4.07	76.56
	Shear modulus (Hill) G	126.59	111.65	36.47	77.18
	Young's modulus (Hill) E	355.48	316.46	107.63	224.67
	Cauchy pressure ($C_{12}-C_{44}$)	151.91	189.93	367.05	393.31
	Kleinman parameter (ζ)	0.54	0.53	0.64	0.68
	Pugh's ratio (B/G)	4.87	5.70	19.88	10.89
	Poisson ratio (ν)	0.40	0.41	0.475	0.455
	Plasticity measurement (B/C_{44})	4.87	6.86	293.62	14.93
	Anisotropy factor (A)	0.63	0.43	0.01	0.33
	Dynamic stability	Stable	Stable	Unstable	Stable

compounds exhibit ductility across the whole pressure range. The decreasing trend of Poisson's ratio in $GeCrO_3$ under pressure may suggest a transition toward a more brittle nature, which could be due to pressure-induced changes in bonding or structure.

The distortion of a material (solid) that experiences irreversible shape changes in response to an applied force is called plasticity in material science.[73] The link between applied pressure and the plasticity of SiCrO, GeCrO, and SnCrO is depicted in Fig. 10 (right). The plasticity of $SiCrO_3$, $GeCrO_3$, and $SnCrO_3$ exhibits a clear dependence on applied pressure, reflecting changes in their mechanical response under stress. For $SiCrO_3$, plasticity increases from 11.07 at 0 GPa to 14.93 at 30 GPa, indicating improved capacity for permanent deformation. $GeCrO_3$ initially shows low plasticity (2.47 at 0 GPa), which rises steadily to 9.86 at 30 GPa, suggesting pressure-induced enhancement in ductility, likely due to changes in bonding or structural arrangement. $SnCrO_3$ follows a similar trend, with plasticity increasing from 4.87 to 14.93 over the same pressure range, pointing to significant improvement in deformability under compression. These trends highlight the potential of these materials for high-pressure applications where mechanical adaptability is critical.[74]

Anisotropy is a crucial parameter for compounds used in engineering applications. A material with an anisotropy value equal to one is considered isotropic, while any other deviation from unity indicates the degree of elastic anisotropy present in the crystal. The value of parameter A for the compounds $ACrO_3$ (A = Si, Ge, Sn) is either less than or higher than unity, making the crystal anisotropic.

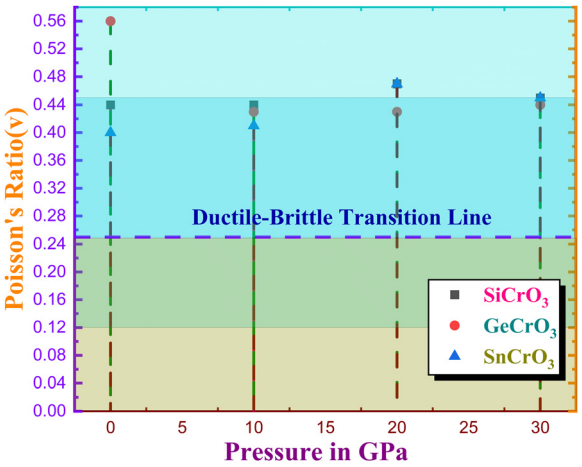

Fig. 11 Ductile-brittle behavior of $ACrO_3$ (A = Si, Ge, Sn) at different pressures.

3.6. Optical properties

Knowing a material's optical characteristics is essential for figuring out its optoelectronic nature. Furthermore, examining optical properties is crucial because semiconductors frequently display metal-like activity at extremely low frequencies and insulating behavior at very high frequencies.[75] Fig. 12(a) and (b) display the computed $\varepsilon_1(\omega)$ and $\varepsilon_2(\omega)$ components of the dielectric function in the pressure range of 0–30 GPa in the 0–30 eV range for $ACrO_3$ (A = Si, Ge, Sn) with electric field polarization vectors along the [100] direction. As the resulting photon energy increased in the low-energy zone, the dielectric functions (both the real part ε_1 and the imaginary part ε_2) were significantly lowered, as shown in Fig. 12(a). The observed dielectric constant trend suggests that the compounds under investigation are appropriate for use in microelectronic applications and integrated circuits.[76] The dielectric function is a complex function that is given by ref. 77:

$$\varepsilon(\omega) = \varepsilon_1(\omega) + i\varepsilon_2(\omega) \quad (17)$$

One of the key properties of half-metallic materials is the plasma frequency, ω_p. It has a real component of the dielectric function with zero value.[77] Based on Fig. 12(a), we can see that $SiCrO_3$ and $GeCrO_3$ have zero values of ε_1 over the entire pressure range in the ultraviolet region at 5–10 eV. In contrast, $SnCrO_3$ also has zero values of ε_1 in the visible energy range for 10–30 GPa and at pressures of 0 to 20 GPa in the ultraviolet region, where transitions occur from metallic to dielectric. In the IR spectrum region, the real component of the dielectric function shows a distinctive peak. The intra-band Drude-like characteristic of $ACrO_3$ (A = Si, Ge, Sn) is the negative frequency of the real part of the dielectric function. The imaginary part of the dielectric function has a value that is very close to zero, and the real part tends to be united in the high-energy zone. It verifies that the material is optically isotropic by presenting it as a virtually transparent substance with minimal absorption in the infrared spectrum. The static dielectric constant $\varepsilon_1(0)$ for $SnCrO_3$ $\varepsilon_1(0)$ at pressures 0, 10, 20, and 30 GPa are 0.5, 5, 5.3 and 5.5 eV, respectively $SnCrO_3$. It is evident from Fig. 12(a) and (b) that the real and imaginary components of the dielectric functions both have relatively greater values at low energies and begin to decline as energy increases.

Refractive index $n(\omega)$ is a crucial optical characteristic that may be found in terms of the complex dielectric function as shown in ref. 78:

$$n(\omega) = \frac{1}{\sqrt{2}}\left(\varepsilon_1 + \left(\varepsilon_1^2 + \varepsilon_2^2\right)^{\frac{1}{2}}\right)^{1/2} \quad (18)$$

The spectrum of refractive index with incident energy is displayed in Fig. 12(c). The presence of free electrons in metallic compounds is responsible for the maximum value of the $ACrO_3$ (A = Si, Ge, Sn) refractive index in the low-energy regions. For $SiCrO_3$ and $GeCrO_3$, the refractive index shows significant peaks in the visible energy range, remains approximately constant across the complete pressure range, and gradually drops in the ultraviolet energy region. $SnCrO_3$ has refractive index peaks in the infrared region and progressively drops in the visible and ultraviolet wavelength ranges.

The optical conductivity $\sigma(\omega)$ of $ACrO_3$ (A = Si, Ge, Sn) is shown in Fig. 12(d). It is an important optical parameter that may be expressed as follows:

$$\sigma(\omega) = \frac{W_{CV}h}{E_0^2} \quad (19)$$

where W_{CV} is the transition probability per unit of time.[79] Fig. 12(d) shows that for $SiCrO_3$ and $GeCrO_3$, conductivity increases quickly in the visible zone and reaches its maximum value in the ultraviolet range as incident energy increases. $SiCrO_3$ and $GeCrO_3$ have the highest conductivity among these compounds at 20 GPa, with no peaks seen in the visible or infrared spectrum. The spectrum for $SnCrO_3$ differs significantly from those of the other compounds, with two minor peaks occurring in the energy ranges of 4.8–7.5 eV and 1–2.5 eV. For the second significant peak, the conductivity in the ultraviolet energy region increases as pressure rises. Because of the hybridization of the valence and conduction bands, conductivity begins at zero photon energy, indicating that there is no band gap at the Fermi level for the up channel, which was confirmed during the investigation of the DOS.

The absorption coefficient $I(\omega)$ spectra for $ACrO_3$ (A = Si, Ge, Sn) are shown in Fig. 12(e). This spectrum gives information on light absorption and the final disappearance of an incident electromagnetic beam that passes through an absorbing material. In the infrared region, at 0 and 30 GPa, compounds $ACrO_3$ (A = Si, Ge, Sn) absorb incident light and show semiconducting characteristics. When the pressure increases, the first noticeable peaks for $SiCrO_3$ and $GeCrO_3$ are seen in the 6–9 eV energy range. These peaks move to the right with increasing pressure. $SnCrO_3$, on the other hand, has a modest peak in the infrared region and reaches its most significant value in the ultraviolet. $ACrO_3$ (A = Si, Ge, Sn) show recurrent peaks in the 10–20 eV energy region. The absorption edge was altered with pressure because of the decrease in the band gap. Our analysis

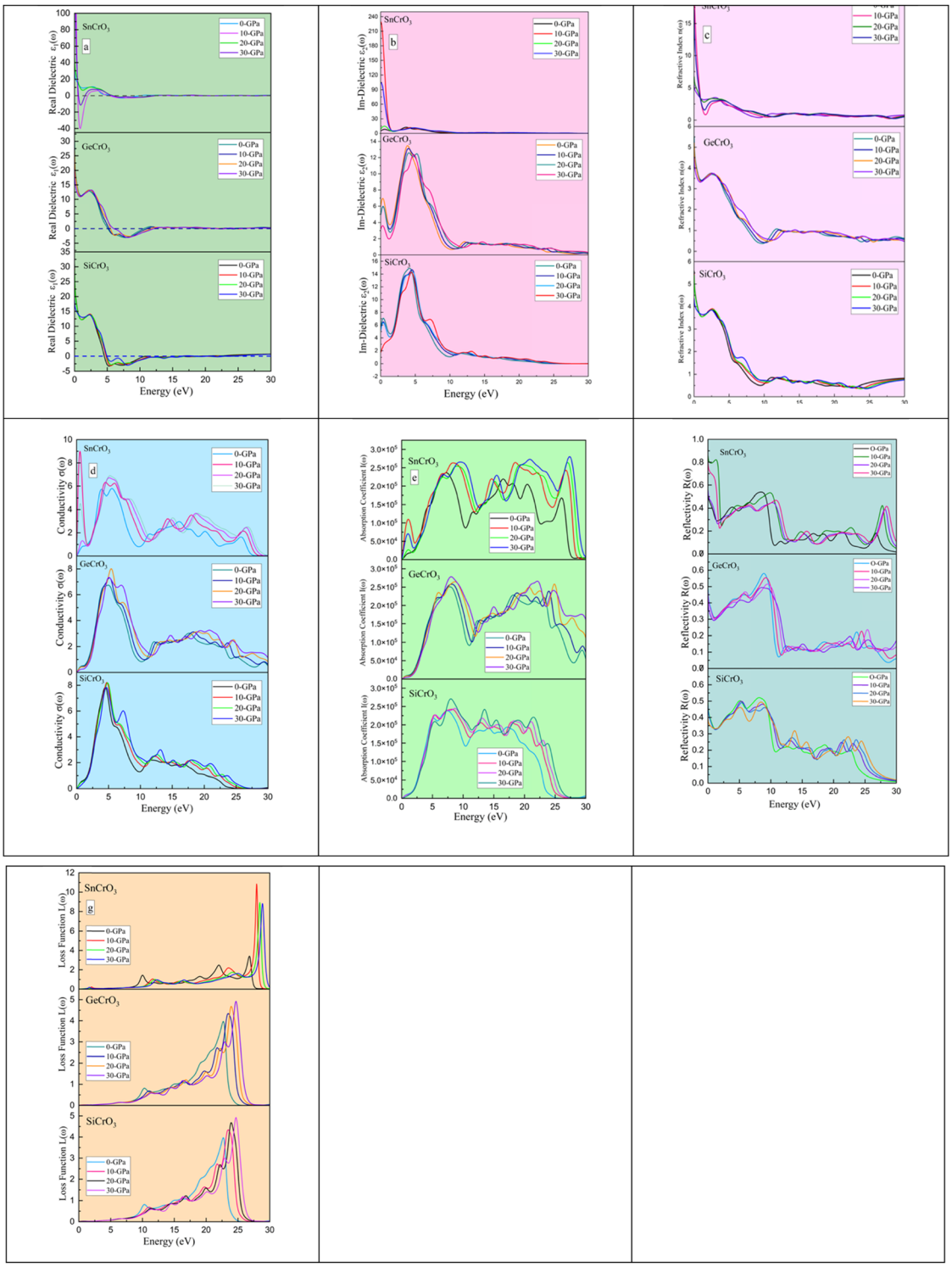

Fig. 12 Energy-dependent optical parameters of $ACrO_3$ (A = Si, Ge, Sn) at various pressures. (a) Real, (b) imaginary part of dielectric function, (c) refractive index, (d) conductivity, (e) absorption co-efficient, (f) reflectivity and (g) loss function.

shows that $SnCrO_3$ has an excellent absorption coefficient in the high-energy range, with the most prominent peaks occurring at 27.5 eV.

Reflectivity is the ratio of incident power to reflected power. It describes a material surface characteristic and is calculated using the following equation[80],

$$R(\omega) = \left| \frac{\sqrt{\varepsilon(\omega)} - 1}{\sqrt{\varepsilon(\omega)} + 1} \right|^2 \quad (20)$$

Fig. 12(f) shows the reflectivity as a function of incident energy. $SiCrO_3$ and $GeCrO_3$ have reflectivity of between 40 and 45% at zero-incident energy, and their spectra are nearly identical. The reflectivity decreases in the visible energy range before increasing to a high of roughly 48% at 0 GPa and a roughly constant value of 50% between 0 and 30 GPa. For $SnCrO_3$, reflectivity starts from 0.51, 0.78, and 0.85 eV at 0, 10, 20 and 30 GPa, respectively, for zero-incident energy. Reflectivity falls significantly with increasing incident energy at 10 and 30 GPa, dropping by about 55%, and at 0 and 10 GPa. A reduction of about 30% within the visible energy range, prior to reaching 1.5 eV, with some minor fluctuations in the 4–7 eV range. In the ultraviolet radiation range, the maximum reflectance is roughly 52% for 0 and 10 GPa and 44% and 46% for 20 and 30 GPa, respectively. It is seen that the reflectivity peaks for all the compounds shift to the right, undergoing a significant form change as pressure increases from 0 to 30 GPa. Fig. 12(f) reveals that $ACrO_3$ (A = Si, Ge, Sn) is not a good reflector in the visible region, and the $R(0)$ value is relatively high in the IR region compared to other areas. Thus, $ACrO_3$ (A = Si, Ge, Sn) can be used in IR mirrors as a coating for optical instruments.[81] The loss per unit area resulting from heating, plasma resonance, and scattering is measured by the optical energy loss factor $L(\omega)$. The electron energy loss function $L(\omega)$ can be obtained from the real and imaginary components of the complex dielectric function:

$$L(\omega) = \left(\frac{\varepsilon_2(\omega)}{\varepsilon_1{}^2(\omega) + \varepsilon_2{}^2(\omega)}\right) \quad (21)$$

Fig. 12(g) illustrates the electron energy loss spectrum (EELS). We observed negligible energy loss of electrons for $ACrO_3$ (A = Si, Ge, Sn) compounds in the IR and visible energy ranges. The significant losses occur in the ultraviolet energy region (25–30 eV). Therefore, from the energy loss spectra, the significant peaks of plasmon energy (a collective oscillation of valence electron energy) for $SnCrO_3$ are situated at 27, 27.5, 28 and 29 eV, respectively, at 0, 10, 20, and 30 GPa$SnCrO_3$, which indicates that the plasmon energy spectrum moves towards the higher energy region as pressure increases. Similar features were observed for $SiCrO_3$ and $GeCrO_3$, where major peaks move toward the right with increasing pressure. The highest peak in the energy loss spectrum occurs because of bulk plasmonic excitation. This happens at a specific incident photon energy and its corresponding frequency, known as the bulk plasma frequency.[82] Rather than absorbing high-energy photons, we detected some modest peaks in the energy range of 15–20 eV, which suggest surface plasmonic excitations at the metal–dielectric interface due to optical transition. This loss spectroscopy indicated that the substances can be used for non-linear optics, biosensors, near-field optics (light guiding below the diffraction limit), and other applications.[83]

4. Conclusion

In this study, we used the DFT framework with a GGA to investigate $ACrO_3$ (A = Si, Ge, Sn) compounds. Our results were consistent with those reported in the literature. We found that the lattice constant and bond length decrease with increasing hydrostatic pressure. The investigated substances retained their cubic phases over a range of pressures. Determining the tolerance factor confirmed the stability of the cubic phase under different pressure regimes. $ACrO_3$ (A = Si, Ge, Sn) was found to be a half-metal based on spin-polarized electronic band structures, the DOS, and the integer value of the magnetic moment (μ_B) per unit cell. We observed that the structure is more stable in the ferromagnetic state than in the non-magnetic state. An analysis of Mulliken charges showed that $ACrO_3$ (A = Si, Ge, Sn) exhibits covalent and ionic bonding behavior. $SnCrO_3$ exhibited metallic behavior at the critical lattice constant after losing its integer magnetic moment, while the other compounds maintained constant magnetic moments. We also examined the ductile and brittle behavior and bonding characteristics of the compounds using Poisson's ratios. Our analysis indicated that $SiCrO_3$ and $SnCrO_3$ are brittle at 0 and 10 GPa and ductile in other pressure regions, while $GeCrO_3$ exhibited ductile behavior at all pressures. The Kleinman parameter decreased linearly, suggesting a decrease in plasticity with pressure. Additionally, we investigated the optical behavior of $ACrO_3$ (A = Si, Ge, Sn) by calculating the dielectric function, refractive index, optical conductivity, absorption, reflectivity, and energy loss function. We observed maximum absorption and minimum energy loss in the ultraviolet region. The real and imaginary parts of the dielectric function showed that the compound is metallic in the infrared and visible range, while exhibiting semiconducting behavior in the ultraviolet energy region. As there is no literature data available for these $ACrO_3$ (A = Si, Ge, Sn) materials, the data reported in this study can serve as a reference for future research and will be valuable for understanding and developing effective optoelectronic and spintronics devices.

Conflicts of interest

The authors declare that they have no conflicts of interest.

Data availability

The data supporting this article have been included as part of the ESI.†

Acknowledgements

We thankfully acknowledge the Ministry of Science and Technology, Bangladesh for their financial support in this project conducted by the members of the Condensed Matter Physics lab at Jahangirnagar University through their R&D fund allocation program. We are also thankful to the Jahangirnagar University-funded Project for the financial assistance to conduct the research work in the Computational Physics (CP) Research Lab in the Department of Physics at Jahangirnagar University.

References

1 J. Fabian, A. Matos-Abiague, C. Ertler, P. Stano and I. Zutic, Semiconductor Spintronics, *Acta Phys. Slovaca*, 2007, **57**, 659–700, DOI: 10.2478/v10155-010-0086-8.

2 D. D. Awschalom and M. E. Flatté, Challenges for semiconductor spintronics, *Nat. Phys.*, 2007, **3**, 153–159, DOI: 10.1038/NPHYS551KWRD=PHYSICS.

3 V. Baltz, A. Manchon, M. Tsoi, T. Moriyama, T. Ono and Y. Tserkovnyak, Antiferromagnetic spintronics, *Rev. Mod. Phys.*, 2018, **90**, 015005, DOI: 10.1103/REVMODPHYS.90.015005/FIGURES/48/THUMBNAIL.

4 P. Chongthanaphisut, K. J. Lee, S. Lee, X. Liu, M. Dobrowolska and J. K. Furdyna, Gate control of interlayer exchange coupling in ferromagnetic semiconductor trilayers with perpendicular magnetic anisotropy, *APL Mater.*, 2022, **10**, 041102, DOI: 10.1063/5.0079245.

5 R. Lebrun, A. Ross, S. A. Bender, A. Qaiumzadeh, L. Baldrati, J. Cramer, A. Brataas, R. A. Duine and M. Kläui, Tunable long-distance spin transport in a crystalline antiferromagnetic iron oxide, *Nature*, 2018, **561**, 222–225, DOI: 10.1038/S41586-018-0490-7.

6 X. Yang, Z. Zhou, T. Nan, Y. Gao, G. M. Yang, M. Liu and N. X. Sun, Recent advances in multiferroic oxide heterostructures and devices, *J. Mater. Chem. C*, 2015, **4**, 234–243, DOI: 10.1039/C5TC03008K.

7 S. Heo, S. K. Sharma, S. Lee, Y. Lee, C. Kim, B. Lee, H. Lee and D. Y. Kim, Effects of y contents on surface, structural, optical, and electrical properties for Y-doped ZnO thin films, *Thin Solid Films*, 2014, **558**, 27–30, DOI: 10.1016/J.TSF.2014.02.025.

8 S. Baturay, Y. S. Ocak and D. Kaya, The effect of Gd doping on the electrical and photoelectrical properties of Gd:ZnO/p-Si heterojunctions, *J. Alloys Compd.*, 2015, **645**, 29–33, DOI: 10.1016/J.JALLCOM.2015.04.212.

9 S. Chen, L. Lin, J. Liu, P. Lv, X. Wu, W. Zheng, Y. Qu and F. Lai, An electrochemical constructed p-Cu_2O/n-ZnO heterojunction for solar cell, *J. Alloys Compd.*, 2015, **644**, 378–382, DOI: 10.1016/J.JALLCOM.2015.02.230.

10 Magnetoelectric Spin Wave Modulator Based On Synthetic Multiferroic Structure, – Abstract – Europe PMC, (n.d.), https://europepmc.org/article/pmc/pmc6052081 (accessed June 15, 2025).

11 S. Sharma, A. Paliwal, M. Tomar and V. Gupta, Multiferroic BFO/BTO multilayer structures based magnetic field sensor, *Phys. B*, 2019, **571**, 1–4, DOI: 10.1016/J.PHYSB.2019.06.056.

12 (PDF) Multiferroic materials for sensors, transducers and memory devices, (n.d.), https://www.researchgate.net/publication/237010601_Multiferroic_materials_for_sensors_transducers_and_memory_devices (accessed June 15, 2025).

13 M. M. Vopson, Fundamentals of multiferroic materials and their possible applications, *Crit. Rev. Solid State Mater. Sci.*, 2015, **40**, 223–250, DOI: 10.1080/10408436.2014.992584.

14 Z. Zanolli, Graphene-multiferroic interfaces for spintronics applications, *Sci. Rep.*, 2016, **1**(6), 1–6, DOI: 10.1038/srep31346.

15 W. E. Pickett and J. S. Moodera, Half Metallic Magnets, *Phys. Today*, 2001, **54**, 39–44, DOI: 10.1063/1.1381101.

16 I. Galanakis, P. H. Dederichs and N. Papanikolaou, Slater-Pauling behavior and origin of the half-metallicity of the full-Heusler alloys, *Phys. Rev. B: Condens. Matter Mater. Phys.*, 2002, **66**, 174429, DOI: 10.1103/PhysRevB.66.174429.

17 R. A. de Groot, Half-metallic magnetism, *Europhys. News*, 1992, **23**, 146–148, DOI: 10.1051/epn/19922308146.

18 I. Galanakis and P. Mavropoulos, Zinc blende compounds of transition elements with N, P, As, Sb, S, Se, and Te as half-metallic systems, *Phys. Rev. B: Condens. Matter Mater. Phys.*, 2003, **67**, 104417, DOI: 10.1103/PhysRevB.67.104417.

19 J. Dho, S. Ki, A. F. Gubkin, J. M. S. Park and E. A. Sherstobitova, A neutron diffraction study of half-metallic ferromagnet CrO_2 nanorods, *Solid State Commun.*, 2010, **150**, 86–90, DOI: 10.1016/J.SSC.2009.09.044.

20 S. Soeya, J. Hayakawa, H. Takahashi, K. Ito, C. Yamamoto, A. Kida, H. Asano and M. Matsui, Development of half-metallic ultrathin Fe_3O_4 films for spin-transport devices, *Appl. Phys. Lett.*, 2002, **80**, 823–825, DOI: 10.1063/1.1446995.

21 A. Amudhavalli, R. Rajeswarapalanichamy and K. Iyakutti, Half metallic ferromagnetism in Ni based half Heusler alloys, *Comput. Mater. Sci.*, 2018, **148**, 87–103, DOI: 10.1016/J.COMMATSCI.2018.02.026.

22 Y. W. Son, M. L. Cohen and S. G. Louie, Half-metallic graphene nanoribbons, *Nature*, 2006, **444**, 347–349, DOI: 10.1038/NATURE05180.

23 S. Ali, H. Ullah, A. A. AlObaid and T. I. Al-Muhimeed, Crystal field splitting, half metallic ferromagnetism, structural, mechanical and magneto-electronic properties of spinels type structure compounds MgX_2O_4 (X = Fe and Co) for spintronic applications, *Eur. Phys. J. Plus*, 2021, **136**, 770, DOI: 10.1140/EPJP/S13360-021-01737-W.

24 B. G. Liu, Robust half-metallic ferromagnetism in zinc blende CrSb, *Phys. Rev. B: Condens. Matter Mater. Phys.*, 2003, **67**, 172411, DOI: 10.1103/PhysRevB.67.172411.

25 R. A. De Groot, F. M. Mueller, P. G. V. Engen and K. H. J. Buschow, New Class of Materials: Half-Metallic Ferromagnets, *Phys. Rev. Lett.*, 1983, **50**, 2024, DOI: 10.1103/PhysRevLett.50.2024.

26 N. A. Benedek and C. J. Fennie, Why are there so few perovskite ferroelectrics?, *J. Phys. Chem. C*, 2013, **117**, 13339–13349, DOI: 10.1021/JP402046T/SUPPL_FILE/JP402046T_SI_001.PDF.

27 C. J. Fennie, Ferroelectrically Induced Weak Ferromagnetism by Design, *Phys. Rev. Lett.*, 2008, **100**, 167203, DOI: 10.1103/PHYSREVLETT.100.167203/FIGURES/3/THUMBNAIL.

28 I. A. Sergienko and E. Dagotto, Role of the Dzyaloshinskii-Moriya interaction in multiferroic perovskites, *Phys. Rev. B: Condens. Matter Mater. Phys.*, 2006, **73**, 094434, DOI: 10.1103/PHYSREVB.73.094434/FIGURES/5/THUMBNAIL.

29 T. Moriya, Anisotropic Superexchange Interaction and Weak Ferromagnetism, *Phys. Rev.*, 1960, **120**, 91, DOI: 10.1103/PhysRev.120.91.

30 I. Dzyaloshinsky, A thermodynamic theory of "weak" ferromagnetism of antiferromagnetics, *J. Phys. Chem. Solids*, 1958, **4**, 241–255, DOI: 10.1016/0022-3697(58)90076-3.

31 S. Esposito and A. Naddeo, The Genesis of the Quantum Theory of the Chemical Bond, *Adv. Historical Studies*, 2014, **03**, 229–257, DOI: **10.4236/AHS.2014.35020**.

32 J. B. Goodenough and J. Zhou, Varied roles of Pb in transition-metal $PbMO_3$ perovskites (M = Ti, V, Cr, Mn, Fe, Ni, Ru), *Sci. Technol. Adv. Mater.*, 2015, **16**, 036003, DOI: **10.1088/1468-6996/16/3/036003**.

33 L. H. da, S. Lacerda and S. R. de Lazaro, Multiferroism and magnetic ordering in new $NiBO_3$ (B = Ti, Ge, Zr, Sn, Hf and Pb) materials: a DFT study, *J. Magn. Mater.*, 2018, **465**, 412–420, DOI: **10.1016/J.JMMM.2018.06.029**.

34 S. Jena, S. Bhattacharya and S. Datta, Signature of half-metallicity in $BiFeO_3$: a DFT study, *Comput. Mater. Sci.*, 2022, **204**, 111107, DOI: **10.1016/J.COMMATSCI.2021.111107**.

35 R. Anar and S. Nazir, Exploring multiferroicity, half-metallic phase, and Curie temperature in X = B/C/N/F-Doped $KNbO_3$: a DFT aspect, *Phys. Scr.*, 2024, **99**, 035907, DOI: **10.1088/1402-4896/AD21C8**.

36 Y. Fang, M. Li and F. Chen, Observation of Magnetic Phase Transition and Magnetocaloric Effect in $Ba_{1-x}Sr_xMnO_{3-\delta}$, *J. Supercond. Novel Magn.*, 2018, **31**, 3787–3792, DOI: **10.1007/s10948-018-4648-1**.

37 S. Yoon, K. Son, S. G. Ebbinghaus, M. Widenmeyer and A. Weidenkaff, Ferromagnetism in nitrogen and fluorine substituted $BaTiO_3$, *J. Alloys Compd.*, 2018, **749**, 628–633, DOI: **10.1016/J.JALLCOM.2018.03.221**.

38 Z. H. Zhu and X. H. Yan, Half-metallic properties of perovskite $BaCrO_3$ and $BaCr_{0.5}Ti_{0.5}O_3$ superlattice: LSDA+*U* calculations, *J. Appl. Phys.*, 2009, **106**, 023713, DOI: **10.1063/1.3182721/393660**.

39 P. K. Gupta, S. Ghosh, A. Pal, S. Roy, A. G. Joshi, A. K. Ghosh and S. Chatterjee, Study of band structure, transport and magnetic properties of $BiFeO_3$–$TbMnO_3$ composite, *SN Appl. Sci.*, 2019, **1**, 1607, DOI: **10.1007/s42452-019-1640-8**.

40 M. tariq, A. Shaari, K. Chaudhary, R. Ahmed, M. A. Jalilj and F. D. Ismail, Magnetoelectric, and Dielectric Switching Properties of Co-Doped $Bifeo_3$ for Low Energy Memory Technology: A First-Principles Study, *SSRN Electron. J.*, 2022, DOI: **10.2139/SSRN.4223051**.

41 J. P. Perdew and A. Zunger, Self-interaction correction to density-functional approximations for many-electron systems, *Phys. Rev. B: Condens. Matter Mater. Phys.*, 1981, **23**, 5048, DOI: **10.1103/PhysRevB.23.5048**.

42 D. M. Ceperley and B. J. Alder, Ground State of the Electron Gas by a Stochastic Method, *Phys. Rev. Lett.*, 1980, **45**, 566, DOI: **10.1103/PhysRevLett.45.566**.

43 M. D. Segall, P. J. D. Lindan, M. J. Probert, C. J. Pickard, P. J. Hasnip, S. J. Clark and M. C. Payne, First-principles simulation: ideas, illustrations and the CASTEPcode, *J. Phys.: Condens. Matter*, 2002, **14**, 2717, DOI: **10.1088/0953-8984/14/11/301**.

44 B. G. Pfrommer, M. Côté, S. G. Louie and M. L. Cohen, Relaxation of Crystals with the Quasi-Newton Method, *J. Comput. Phys.*, 1997, **131**, 233–240, DOI: **10.1006/JCPH.1996.5612**.

45 M. C. Payne, M. P. Teter, D. C. Allan, T. A. Arias and J. D. Joannopoulos, Iterative minimization techniques for *ab initio* total-energy calculations: molecular dynamics and conjugate gradients, *Rev. Mod. Phys.*, 1992, **64**, 1045, DOI: **10.1103/RevModPhys.64.1045**.

46 S. M. Hosseini, T. Movlarooy and A. Kompany, First-principle calculations of the cohesive energy and the electronic properties of $PbTiO_3$, *Phys. B*, 2007, **391**, 316–321, DOI: **10.1016/J.PHYSB.2006.10.013**.

47 B. Ghebouli, M. A. Ghebouli and M. Fatmi, Structural, elastic, electronic, optical and thermal properties of cubic perovskite $CsCdF_3$ under pressure effect, *Eur. Phys. J.: Appl. Phys.*, 2011, **53**, 30101, DOI: **10.1051/EPJAP/2010100318**.

48 M. Segall, R. Shah, C. Pickard and M. Payne, Population analysis of plane-wave electronic structure calculations of bulk materials, *Phys. Rev. B: Condens. Matter Mater. Phys.*, 1996, **54**, 16317, DOI: **10.1103/PhysRevB.54.16317**.

49 Z. Ali, I. Ahmad, B. Khan and I. Khan, Robust Half-Metallicity and Magnetic Properties of Cubic Perovskite $CaFeO_3$, *Chin. Phys. Lett.*, 2013, **30**, 047504, DOI: **10.1088/0256-307X/30/4/047504**.

50 Z. Ali, I. Ahmad, B. Amin, M. Maqbool, G. Murtaza, I. Khan, M. J. Akhtar and F. Ghaffor, Theoretical studies of structural and magnetic properties of cubic perovskites $PrCoO_3$ and $NdCoO_3$, *Phys. B*, 2011, **406**, 3800–3804, DOI: **10.1016/J.PHYSB.2011.06.065**.

51 S. A. Khandy and D. C. Gupta, DFT analogue of prospecting the spin-polarised properties of layered perovskites Ba_2ErNbO_6 and Ba_2TmNbO_6 influenced by electronic structure, *Sci. Rep.*, 2022, **12**, 1–14, DOI: **10.1038/S41598-022-22070-X**.

52 P. Dufek, P. Blaha and K. Schwarz, Applications of Engel and Vosko's generalized gradient approximation in solids, *Phys. Rev. B: Condens. Matter Mater. Phys.*, 1994, **50**, 7279, DOI: **10.1103/PhysRevB.50.7279**.

53 D. Koller, F. Tran and P. Blaha, Improving the modified Becke-Johnson exchange potential, *Phys. Rev. B: Condens. Matter Mater. Phys.*, 2012, **85**, 155109, DOI: **10.1103/PHYSREVB.85.155109/FIGURES/6/THUMBNAIL**.

54 P. Nayak and D. C. Gupta, Exploring the multifaceted properties: electronic, magnetic, Curie temperature, elastic, thermal, and thermoelectric characteristics of gadolinium-filled $PtSb_3$ skutterudite, *RSC Adv.*, 2024, **14**, 17364–17379, DOI: **10.1039/D4RA01303D**.

55 J. M. Leger, C. Loriers-Susse and B. Vodar, Pressure Effect on the Curie Temperatures of Transition Metals and Alloys, *Phys. Rev. B: Condens. Matter Mater. Phys.*, 1972, **6**, 4250, DOI: **10.1103/PhysRevB.6.4250**.

56 B. Aladerah, M. Gharaibeh, A. Obeidat and K. Aledealat, A comparative study of structural, electronic, magnetic, and pressure-dependent properties of Full-Heusler Fe_2XSi (X = Mn and Co): first-principles calculation and Monte Carlo Simulation, *Phys. Scr.*, 2023, **98**, 085954, DOI: **10.1088/1402-4896/ACE8CE**.

57 W. Chen, J. George, J. B. Varley, G. M. Rignanese and G. Hautier, High-throughput computational discovery of $In_2Mn_2O_7$ as a high Curie temperature ferromagnetic semiconductor for spintronics, *npj Comput. Mater.*, 2019, **5**, 1–7, DOI: **10.1038/S41524-019-0208-X**.

58 N. Moulay, M. Ameri, Y. Azaz, A. Zenati, Y. Al-Douri and I. Ameri, Predictive study of structural, electronic, magnetic and thermodynamic properties of $XFeO_3$ (X = Ag, Zr and Ru) multiferroic materials in cubic perovskite structure: first-principles calculations, *Mater. Sci.*, 2015, **33**, 402–413, DOI: 10.1515/MSP-2015-0047.

59 Z. Ali, I. Ahmad, B. Khan and I. Khan, Robust Half-Metallicity and Magnetic Properties of Cubic Perovskite $CaFeO_3$, *Chin. Phys. Lett.*, 2013, **30**, 047504, DOI: 10.1088/0256-307X/30/4/047504.

60 A. Jabar, S. Benyoussef and L. Bahmad, Study of Physical Characteristics of the New Half-Heusler Alloy BaHgSn by DFT Analysis, 2024, https://arxiv.org/pdf/2403.08483 (accessed June 15, 2025).

61 R. A. De Groot, F. M. Mueller, P. G. V. Engen and K. H. J. Buschow, New Class of Materials: Half-Metallic Ferromagnets, *Phys. Rev. Lett.*, 1983, **50**, 2024, DOI: 10.1103/PhysRevLett.50.2024.

62 R. K. Pingak, S. Bouhmaidi, L. Setti, B. Pasangka, B. Bernandus, H. I. Sutaji, F. Nitti and M. Z. Ndii, Structural, Electronic, Elastic, and Optical Properties of Cubic $BaLiX_3$ (X = F, Cl, Br, or I) Perovskites: An Ab-initio DFT Study, *Indones. J. Chem.*, 2023, **23**, 843–862, DOI: 10.22146/IJC.83261.

63 Z. J. Wu, E. J. Zhao, H. P. Xiang, X. F. Hao, X. J. Liu and J. Meng, Crystal structures and elastic properties of superhard Ir N_2 and Ir N_3 from first principles, *Phys. Rev. B: Condens. Matter Mater. Phys.*, 2007, **76**, 054115, DOI: 10.1103/PHYSREVB.76.054115/FIGURES/12/THUMBNAIL.

64 S. Goumri-Said and M. B. Kanoun, Theoretical investigations of structural, elastic, electronic and thermal properties of Damiaoite $PtIn_2$, *Comput. Mater. Sci.*, 2008, **43**, 243–250, DOI: 10.1016/J.COMMATSCI.2007.10.009.

65 J. Gao, Q. J. Liu and B. Tang, Elastic stability criteria of seven crystal systems and their application under pressure: taking carbon as an example, *J. Appl. Phys.*, 2023, **133**, 135901, DOI: 10.1063/5.0139232.

66 M. J. Mehl, Pressure dependence of the elastic moduli in aluminum-rich Al-Li compounds, *Phys. Rev. B: Condens. Matter Mater. Phys.*, 1993, **47**, 2493, DOI: 10.1103/PhysRevB.47.2493.

67 Z. Sun, S. Li, R. Ahuja and J. M. Schneider, Calculated elastic properties of M_2AlC (M = Ti, V, Cr, Nb and Ta), *Solid State Commun.*, 2004, **129**, 589–592, DOI: 10.1016/J.SSC.2003.12.008.

68 C. Jasiukiewicz and V. Karpus, Debye temperature of cubic crystals, *Solid State Commun.*, 2003, **128**, 167–169, DOI: 10.1016/J.SSC.2003.08.008.

69 P. Wachter, M. Filzmoser and J. Rebizant, Electronic and elastic properties of the light actinide tellurides, *Phys. B*, 2001, **293**, 199–223, DOI: 10.1016/S0921-4526(00)00575-5.

70 M. J. Mehl, J. E. Osburn, D. A. Papaconstantopoulos and B. M. Klein, Structural properties of ordered high-melting-temperature intermetallic alloys from first-principles total-energy calculations, *Phys. Rev. B: Condens. Matter Mater. Phys.*, 1990, **41**, 10311, DOI: 10.1103/PhysRevB.41.10311.

71 R. Majumder, M. M. Hossain and D. Shen, First-principles study of structural, electronic, elastic, thermodynamic and optical properties of LuPdBi half-Heusler compound, *Mod. Phys. Lett. B*, 2019, **33**(30), 1950378, DOI: 10.1142/S0217984919503780.

72 M. A. Ali, R. Ullah, S. A. Dar, G. Murtaza, A. Khan and A. Mahmood, Modeling of structural, elastic, mechanical, acoustical, electronic and thermodynamic properties of $XPdF_3$ (X = Rb, Tl) perovskites through density functional theory, *Phys. Scr.*, 2020, **95**, 075705, DOI: 10.1088/1402-4896/AB8EEE.

73 L. Vitos, P. A. Korzhavyi and B. Johansson, Stainless steel optimization from quantum mechanical calculations, *Nat. Mater.*, 2003, **2**, 25–28, DOI: 10.1038/NMAT790.

74 X. Q. Chen, H. Niu, D. Li and Y. Li, Modeling hardness of polycrystalline materials and bulk metallic glasses, *Intermetallics*, 2011, **19**, 1275–1281, DOI: 10.1016/J.INTERMET.2011.03.026.

75 G. Dresselhaus, The Fermi surface and optical properties of copper, *Solid State Commun.*, 1969, **7**, 419–423, DOI: 10.1016/0038-1098(69)90887-4.

76 R. Majumder, M. M. Hossain and D. Shen, First-principles study of structural, electronic, elastic, thermodynamic and optical properties of LuPdBi half-Heusler compound, *Mod. Phys. Lett. B*, 2019, **33**, 1950378, DOI: 10.1142/S0217984919503780.

77 M. K. Butt, M. Yaseen, J. Iqbal, A. S. Altowyan, A. Murtaza, M. Iqbal and A. Laref, Structural, electronic, half –metallic ferromagnetic and optical properties of cubic $MAlO_3$ (M = Ce, Pr) perovskites: A DFT study, *J. Phys. Chem. Solids*, 2021, **154**, 110084, DOI: 10.1016/J.JPCS.2021.110084.

78 Oxford Master Series in Condensed Matter Physics Atomic, Optical, and Laser Physics Particle Physics, Astrophysics, and Cosmology, (n.d.), https://global.oup.com/academic/product/optical-properties-of-solids-9780199573363 (accessed June 15, 2025).

79 G. Murtaza and I. Ahmad, First principle study of the structural and optoelectronic properties of cubic perovskites $CsPbM_3$ (M = Cl, Br, I), *Phys. B*, 2011, **406**, 3222–3229, DOI: 10.1016/J.PHYSB.2011.05.028.

80 Electronic structure, chemical bonding, and optical properties of ferroelectric and antiferroelectric | Phys. Rev. B, (n.d.), https://journals.aps.org/prb/abstract/10.1103/PhysRevB.59.1776 (accessed June 15, 2025).

81 B. D. Pennington, Infrared Spectroscopy in Analysis of Polymer Structure–Property Relationships, *Encyclopedia of Analytical Chemistry: Applications, Theory and Instrumentation*, 2000, DOI: 10.1002/9780470027318.A2014.

82 A. Hossain, M. S. I. Sarker, M. K. R. Khan and M. M. Rahman, Spin effect on electronic, magnetic and optical properties of spinel $CoFe_2O_4$: a DFT study, *Mater. Sci. Eng., B*, 2020, **253**, 114496, DOI: 10.1016/J.MSEB.2020.114496.

83 S. Subburaj, B. Arumugam, S. M. Chen, T. W. Chen, A. Seetharam and S. K. Ramaraj, Polyol synthesis of Ag Nanowires as an electrochemical sensor for the quantification of Carcinogenic Hydrazine, *Int. J. Electrochem. Sci.*, 2021, **16**, 210773, DOI: 10.20964/2021.07.74.